Mapping fibre failure in situ in carbon fibre reinforced polymers by fast synchrotron X-ray computed tomography

S.C. Garcea[1,2]*, I. Sinclair[2], S.M. Spearing[2], P.J. Withers[1]

[1] School of Materials, Henry Moseley X-ray Imaging Facility, University of Manchester, Manchester, M13 9PL, United Kingdom
[2] Engineering Materials, University of Southampton, Southampton, SO17 1BJ, United Kingdom

* Corresponding author (serafina.garcea@manchester.ac.uk)

Abstract

Fast, *in situ* synchrotron X-ray computed tomography (CT) has been used to capture damage evolution, particularly fibre failures, before final fracture (within 99.9% of the ultimate tensile stress) in cross-ply carbon fibre/epoxy coupons under continuous monotonic tensile loading for the first time. It is noteworthy that fewer than 8% of the 0° fibres have fractured at 99.9% of the failure load. The majority of fibre breaks appear as isolated events, although some instances of multiple adjacent breaks (clusters) do occur at intermediate and high stress levels. Contrary to conventional wisdom, a cluster of failed fibres would always occur in a burst as a singular failure event: clusters were never seen to accumulate additional broken fibres as load increased suggesting low-level stress concentration local to fibre breaks. Several instances of multiple fractures along individual fibres were observed, providing an estimation of the critical stress transfer length between the fibre and matrix. The factors affecting fibre failure appear to be complex, with distinct sample-to-sample variability being identified for the length-scales tested. This highlights the need for improved understanding of the mechanisms that contribute to final failure, particularly criteria controlling the arrest or otherwise of clustered fracture events.

Keywords: A. Carbon fibres, B. Tensile load, C. Fibre failure, C. Damage mechanics, D. Fast X-ray computed tomography

1. Introduction

Reliable engineering predictions of carbon fibre reinforced polymer (CFRP) structural performance based on physically representative mechanisms are a key to improve CFRP structure design and material development [1]. Such an understanding may help to alleviate the time-consuming and expensive test programmes employed in the contemporary development of primary load-bearing structures. Of the characteristic failure mechanisms of CFRPs, fibre failure is widely identified as critical in unidirectional materials/plies when loaded in tension along the fibre direction. Different approaches have been exploited to predict such fibre-dominated behaviour [1], including analytical models [2-7], statistical models [8-10], and finite element models [11-13]. Such models generally incorporate some allowance for the distribution of individual fibre strengths, the local stress transfer to the fibres from the matrix adjacent to fibre breaks, and, in some cases, the concept of a critical cluster size that triggers final failure [4,14]. Despite the efforts made, contemporary models have only been partially successful in predicting experimental observations for fibre failure, which in themselves are relatively limited within the literature [7,11-13]. Scott *et al.* [15] have previously applied *in situ* CT to visualise the progress of fibre failure of CFRP under incremental loading, clearly showing that fibre breaks occur increasingly at higher loads and that their accumulation follows a power law curve to a good approximation. Clusters of multiple adjacent breaks were associated with high stresses, with the maximum applied stress being ~94% of the ultimate tensile stress (UTS) of the material in question [15]. These results were directly compared with models in Refs. [7,12], highlighting difficulties in predicting cluster formation at high loads [12]. Furthermore, gaps in understanding fibre fracture accumulation processes have been identified, such as the formation of coplanar and dispersed clusters, and the initiation at new locations [7]. Whilst it is evident that CT is a powerful technique for following damage accumulation using both *in situ* and *ex situ* experiments for qualitative and quantitative assessments [16]; previous *in situ* studies of fibre failure under

tension have been characterised by low temporal resolution (~5 minutes per tomograph) with the specimen held constant load during the acquisition of all the projections comprising a scan [15, 17]. Such holds may be anticipated to introduce changes in the material behaviour, particularly in the formation of clusters sustained at high loads [11] and make it difficult to capture the accumulation of fractures within clusters. In addition, given the variability of commercial CFRP coupons, important practical limitations arise in capturing damage events just prior to final failure (within 1% of UTS). Fast synchrotron radiation CT (scan time of 1 s or less) during continuous slow strain rate loading has the potential to overcome these limitations [18-20].

In this study, fast computed tomography was used for the first time to track the accumulation of fibre failure to within one second of final failure, under simple ramp loading representative of standard engineering tensile tests. The combination of continuous monotonic tensile loading, and fast acquisition has allowed: (i) avoidance of potential hold-at-load artefacts, (ii) capture of the sequence and location of successive fibre fracture sites at much finer load steps than reported previously, and (iii) observation of the state of fracture immediately prior to final failure (to within ~0.1% of the sample-specific UTS).

2. Methodology

2.1 Material system

A commercial aerospace-grade thermoplastic particle toughened carbon/epoxy (T700/M21), Hexcel HexPly [21]), with a nominal fibre volume fraction of 60% [15] and a $[90/0]_s$ layup, was studied. Double-edge notched specimens, with a central cross-section between the notches of 1 mm, length of 66 mm and a width of 4 mm were shaped by waterjet cutting from a panel with 1 mm of thickness. Further details of the geometry and coupon dimensions are reported in Ref. [22]. Two coupons are studied in this investigation (identified here as *coupon A* and *coupon B)* to assess the reproducibility of the observed behaviours. It should be noted, that despite the small specimen size, there are more than 7,000 fibres in the 0° plies between

the two notch tips, with a visualised gauge length of ~2 mm over which the fibres breaks are observed (see §2.3 below).

2.2 *In situ* monotonic tensile loading experiments

Uninterrupted rising tensile loading was applied *in situ* upon the CT beamline while the coupons were continuously scanned. Tensile tests were performed using a compact electro-mechanical rig developed by INSA-Lyon [20], specifically designed to be stable at high rotational speeds. The strain rate applied was ~$3x10^{-4}$ /s. The UTS registered was 1400 MPa for coupon A and 1280 MPa for coupon B. These values are higher than that reported for the in previous studies (960 MPa, [17]), which was based on an average of 10 specimens (coefficient of variation of 0.03 [23]). This difference might be mainly related to the smaller cross-section at the notch used in previous studies, reported as 0.7 mm width between notches in Ref. [12]. Final failure was seen to occur at the notch in a catastrophic manner for both coupons considered.

2.3 Fast CT acquisition procedure

Experiments were performed at the Swiss Light Source on the TOMCAT-X02DA Beamline, Paul Scherrer Institut, Villigen, Switzerland. The beam energy used was 20 keV and the distance between the specimen and the detector was set to provide a degree of phase contrast to facilitate the visualisation of small crack-like features [24], such as fibre breaks [25]. The exposure time was set to 2 ms and 500 projections were collected for each tomograph, resulting in 1 tomograph per second. The voxel size was 1.1 μm corresponding to a field of view of ~2.2 x 2.2 mm, sufficient to image the notch region shown in Figure 1. Coupons were initially scanned in the unloaded condition to confirm that no significant damage was introduced during the manufacture. All cutting damage was confined to the near-surface, and as such it was readily excluded from subsequent internal damage evolution under load. The specimens were then mounted in the rig and loaded in tension. The random access memory (RAM) storage capability of the camera limited the data acquisition to roughly twelve

consecutive scans (6000 projections) of the entire region of interest (2016 x 2016 pixels). In continuous mode the image data was overwritten when the storage capability of the camera was reached. The above settings were also used to obtain information at low and intermediate loads, the difference being that when the scan was stopped only the last volume of the sequence (of 12) was considered. This approach avoids having interruptions during the tensile test to perform intermediate scans in the '*start and stop*' mode. At high loads continuous acquisition was used until final failure of the specimen, giving 10 continuous scans immediately prior to failure for coupon A, and 9 for coupon B. When coupon failure occurred the acquisition was manually stopped and the data downloaded from the camera. The percentage of the sample-specific UTS associated with these final continuous scans was in range of 99.4% - 99.9%. Two types of reconstruction have been considered, based on: (i) conventional X-ray attenuation (edge enhanced in this case by acquisition in the near-field Fresnel regime) and (ii) phase retrieval, via the Paganin method [26]. In house GRIDREC/FFT code was employed in both cases [27].

2.4 Image analysis

Previous work has established that a voxel size of ~1 μm allows individual fibre breaks to be detected in carbon fibre composites [25]. Fast tomography is characterised by a short exposure time and fewer projections per scan, with consequent compromises in signal to noise ratio and effective spatial resolution compared to that which is achievable using conventional settings [25]. Figure 2 illustrates the same cross-section parallel to the load direction using conventional absorption (Figure 2(a)), and Paganin phase reconstruction (Figure 2(b)), without applying any image post processing. Paganin reconstruction enhances the contrast between damage and material (fibres and matrix), but compromises sharpness cf. Figure 2(a). The Paganin reconstruction was seen to be less suited to distinguish small features such as single fibre breaks, but it facilitated the segmentation of more open cracks, such as matrix failure (see Figure 2). As such, the analysis of fibre breaks here used

absorption-based reconstructions, while the Paganin results were used for 3D rendering of the different damage modes before final failure, as shown in Figure 1. Reconstructed volumes were filtered using a median filter, ensuring a degree of edge preservation. An example of the improvements obtained by applying the median filter is provided in Figure 2(c), for the same cross-section as shown in Figure 2(a)-(b). For each coupon the volume of interest for successive scans was first registered using ImageJ to facilitate the correlation of failure sites between subsequent load increments. VGStudio Max 2.1 was used to allow the fibre breaks to be detected and manually counted. The numbers of fibre breaks reported are based on three independent counts for each volume.

3. Results

3.1 Progression of the overall damage in the notch region

Damage modes in the notch region have been described previously for tensile loads up to 94% of the UTS [15]. Here the higher scan rate allows imaging up to 99.9% of the UTS, as shown in Figure 1. The number of transverse ply cracks does not increase over the loading range investigated (see Figure 3), indicating that this damage mode saturates at intermediate load levels (55% UTS). The opening of the transverse ply cracks not directly connected with the delamination did not change considerably with loading, as shown in Figure 3(a)-(c), exhibiting crack opening displacements in the range 5-10 μm. By contrast, the opening of those transverse ply cracks linked to delamination increased significantly, from a few microns (5-10 μm) at intermediate loads to ~200 μm before failure, as shown in Figure 3(b)-(c) and in green in the 3D rendering of Figure 1. Shallow angle fibres bridging between the two flanks of the transverse ply cracks were observed even at high loads. The propagation of the matrix cracks in the 0 plies (0^o ply splits) was not tracked here, being seen to propagate along the loading axis, out of the field of view imaged. Their average crack opening at the notch root was found to increase progressively with load, from 5-10 μm at intermediate loads, to 20-25 μm immediately before failure. Delamination was already present at the lowest load observed

in this study (55% UTS for coupon A and 62% UTS for coupon B). The delamination area increased progressively with load, creating an effectively reduced cross-section of material in the region between the notches, as documented previously [25]. Fibre breaks were detected from intermediate loads onwards, and found to be located in this reduced cross-section (measured as 0.45 mm^2 using CT data) isolated by the delamination, 0^o ply splits and transverse ply cracks. Figure 4 shows the projections of failed fibres through the 0˚ plies thickness with respect to the location of transverse ply cracks and delamination for both coupons studied. No significant correlation was observed between transverse ply cracks and the location of fibre breaks in the 0˚ plies. This is consistent with the observations from a previous study for a carbon/epoxy specimen subjected to tensile loading [15] and under fatigue [25]. By contrast, other work conducted on unidirectional non-crimp glass fibre reinforced composites subjected to fatigue has demonstrated a strong correlation between the location of fibre breaks and the presence of other damage modes (matrix crack) in the neighbouring plies [28,29]. It is important to note that the T700/M21 system has particle toughened interlayers between the plies which are likely to reduce the stress concentrations due to damage in the off-axis plies and between them.

3.2 Accumulation of fibre breaks

A summary of fibre breaks is provided in Table 1 for both coupons. Details of the accumulation of fibre breaks in the final continuous scans were omitted from Table 1 to facilitate the comparison, taking into account only the first (99.4% UTS) and last (99.9% UTS) continuous scan. It is evident that the two samples failed at different loads with different numbers of fibre breaks in the notch region: coupon B failed at a somewhat lower load (1280 N compared to 1400 N for coupon A), being characterised by a lower number of fibre breaks at failure (418 compared to 581 for coupon A). Figure 5 shows the plot of the total number of breaks as a function of the applied nominal stress in the reduced load-bearing section:

- Coupon A appears to accumulate fibre failures somewhat faster at intermediate stresses. The two datasets follow a power law fit over the range of overlap.
- Approximately 7% of the total number of fibre breaks occurs during the final loading step (~99.4 and 99.9% of UTS in each case), see Table 1. This is reasonably consistent with the rate of fibre fracture leading up to these loads suggesting that there is not a dramatic change in final fracture rate from the overall power law fit.

The fact that the percentage of fibre breaks in coupon B increases so significantly at high loads (by 35% from 98 to 99.9% of the UTS) confirms the importance of using continuous fast scanning to capture damage accumulation immediately prior to final failure. These damage events would be missed using static holds. It is noteworthy that in both cases fewer than 8% of the 0° fibres in the imaged volume have fractured at 99.9% of the failure load. The type and the number of fibre breaks detected in the two coupons as a function of percentage of UTS are shown in Figure 6. They are divided into singlets (single fibre break indicated by *S*), clusters of two adjacent breaks (*2-plet*), 3 adjacent breaks (*3-plet*), and up to 10 adjacent breaks (*10-plet*), which was the largest number detected. In this study a cluster was defined as an agglomeration of fibre breaks directly adjacent to one other. This is consistent with the fact that the observed multiple fibre breaks are exclusively co-planar rather than dispersed, in agreement with previous studies on the same material [15]. The majority of breaks occur as singlets at all loading levels, whereas the number of clusters increases with load, as shown in Figure 6(a) and 6(b). The total number of singlets immediately prior to final failure (99.9% of UTS) is very similar for both coupons (339 for coupon A and 331 for coupon B). However, the number of intermediate multiplets ($n \geq 2$) is much fewer in coupon B (~50%), and no large multiplets ($n \geq 5$) were seen, whereas 9 large multiplets ($n \geq 5$) were seen in coupon A at 99.9% UTS. Figure 6(a) shows that three 5-plet clusters and one 7-plet are even present at 85% of the UTS in coupon A; while coupon B exhibits only one 2-plet at 90% of UTS. Nevertheless, the percentage of singlets with respect to the total number of breaks is

somewhat different for the two coupons, as shown in Figure 6(c) and 6(d). Coupon A exhibited a significant number of clusters as a function of UTS (multiple breaks representing ~40% compared to 20% for coupon B).

3.3 Immediately prior to final failure

As noted previously, the fast acquisition allowed to record the damage state just prior to coupon failure, which was monitored from 9-10 s (99.4% of UTS) until 1s prior to coupon failure (99.9% of UTS). The number of additional fibre breaks detected during continuous scanning was 41 for coupon A and 31 for coupon B (see Table 1), with a similar number of additional singlets for both coupons (16 for coupon A and 17 for coupon B) as shown in Figure 6(a) and 6(b). The largest new cluster detected in these continuous scans was a 5-plet for coupon A and a 3-plet for coupon B. Newly initiated breaks always occur in new locations rather than in locations adjacent to where fibres have already failed. Figure 7 shows the 5-plet detected during continuous scans in coupon A at 9, 8 and 1 s prior to final failure for the same cross-section parallel to the loading direction. While no fibre breaks are present 9s before failure, a 5-plet "pops in" within the next second and does not accumulate any more fractures in the remnant life prior to the final failure of the coupon.

3.4 Individual fibre fragmentation

The analysis of the fragmentation of individual fibres along their length was conducted using three simultaneous orthogonal views. Examples of these are illustrated in Figure 8 and Figure 9, where the yellow arrows annotate the sequence of fibre failure for incremental loads corresponding to the same cross-section. Focusing on the fibre that exhibits the first break at 55% UTS in Figure 8(a), the increase in load to 85% UTS causes a second break at a distance of 140 μm from the first, shown in Figure 8(b). A further increase in the load (before coupon failure) results in a third fracture at a distance of 95 μm from the second break, Figure 8(c). For the fibre in Figure 9(a-c) the third axial break occurs between the first two fractures, spaced 460 μm apart at a distance of 135 μm and 325 μm from each respectively.

Unsurprisingly, the number of fragments detected, where a fragment is defined between two axial breaks, increases with the applied load for both coupons. The distance between adjacent breaks within single fibres has been used in previous studies to provide an estimate of the *ineffective length* [15, 30, 31]. The cumulative distribution of the fragment lengths, across all fibres containing more than one break within the field of view in the two coupons, is presented in Figure 10. A total number of 106 fibre fragments (63 in coupon A and 43 in coupon B) were identified within 78 individual fibres (40 in coupon A and 38 in coupon B) to achieve this distribution. The minimum length detected, of 30 μm, is shown in the cross-section reported in Figure 2. It is noticeable that the cumulative distribution in Figure 10 reveals a sharp increase in slope up to a fragment length of 70 μm, and it is approximately linear at higher fragment lengths. Below 70 μm there are relatively few fragments. This suggests that 70 μm may be a reasonable estimate for the *'ineffective length'*, which is consistent with the value reported by Scott *et al.* [15] based on five locations of double breaks associated with the highest load achieved in their work (94% UTS). The maximum number of axial breaks observed on an individual fibre was somewhat different for the two coupons investigated: 8 for coupon A and 3 for coupon B. Figure 11 shows two cross-sections parallel to the loading direction for the fibre that exhibited eight axial breaks. The use of two adjacent cross-sections was dictated from the fibre misalignment. Seven breaks were present at 85% UTS, Figure 11(a), while the additional break was observed before final failure of the coupon, dividing the first fragment (1-2) on the left hand side of Figure 11(a) into two parts with different lengths (240 μm and 160 μm). The neighbouring fibre also shows multiple axial failures (six in this case), the majority of these are also visible in Figure 11. These two multi-fragmented neighbouring fibre have co-planar clusters in common: the break annotated as '*2'* in Figure 11(a) is a shared 5-plet, and the break annotated as '*7'* in Figure 11(b) is a shared 2-plet. This case is not unique in coupon A with a similar response observed between other adjacent fibre pairs. However, coupon B did not exhibit any cases of adjacent fibres with

multiple axial breaks. The presence of multiple breaks on a single fibre may of course be related to the presence of a statistically exceptional fibre containing defects introduced by the manufacturing processes, or local stress concentrations, perhaps due to variations in the interface and fibre/matrix adhesion.

4. Discussion

The use of *in situ* fast computed tomography in continuous acquisition mode has enabled significant new observations of fibre failure. This method allows us to look back at the state immediately prior to failure for the first time. The number of fibre breaks at 99.9% of failure is less than ~8% of the total number of fibres in the loaded region of the specimen. This would be consistent with only involving the low-strength tale of a statistical fibre strength distribution. The mechanism of fibre failure accumulation for this material system was clear; breaks do not successively accumulate at locations with pre-existing failed fibres, but rather new breaks always occurred in new locations. This is in agreement with a previous study on the same material [15]. In the first instance, this may be considered consistent with dynamic stress concentrations having a strong influence on cluster formation [32,33], and also with debonding processes or other reduction in the stress concentration on neighbouring fibres that may occur after initial fracture. This could be possibly caused by a dynamic release of strain energy such as local shock-like process upon fracture of a fibre that in some cases generates fibres fractures in the locality as well. The results obtained in this study have shown a somewhat different behaviour between the two coupons considered even though they were made using the same material system and subjected to the same load. A direct comparison highlighted that:

- Coupon A showed a higher failure load (1400 N versus 1280 N of coupon B)
- Coupon A was able to accommodate more fibre breaks for a given percentage of UTS and a given absolute load. At the same time it showed a higher number of multiple axial fragmentations on individual fibres.

- Coupon A exhibited a higher percentage of clusters (35-40% depending on the load level versus 15-20% of coupon B), which on average form at lower loads than for coupon B (already at 85% UTS for coupon A while coupon B at 98% UTS). The largest cluster size was of a 10-plet for coupon A while in coupon B the maximum was 4.
- In both cases the number of singlets counted before final failure was similar.

It is perhaps surprising that coupon A, which was seen to accommodate a larger number of fibre breaks, promoted more clusters and individual fibre fragmentation, giving a higher failure load. A possible explanation is that the location of some of the clusters might be pre-determined by defects induced during processing that affect adjacent fibres, *e.g*. the introduction of small scratches on the fibre surfaces during tape production or during lay-up, which correlate between several adjacent fibres. This conjecture is supported by the observations of the occasional individual fibres, which experienced more than two breaks along their length within the field of view, and the occurrence of shared clusters. This study suggests that clusters forming at intermediate loads (early clusters) do not simply correlate with premature failure. In contrast, based on the results found, the presence of clusters at intermediate loads might correlate with a higher ultimate strength (*i.e.* in coupon A). In particular the presence of clusters at intermediate loads could promote fibre pull-outs explaining why the two specimens behave differently. In this respect the concept of '*virtual co-planar clusters'* has been recently discussed by Bullegas *et al.* [34]. They used laser engraved micro-cut patterns to promote hierarchical pull-outs ahead of a crack tip with a consequent increase in the translaminar fracture toughness. The same concept was previously proposed by Mirkhalaf *et al*. [35] to induce crack deflection to overcome the brittleness of glass. Further experiments are required to confirm whether the presence of clusters at intermediate loads promotes specific mechanisms, such as pull-outs.

Various researchers have discussed the presence of a critical cluster size as being needed to trigger catastrophic failure [4,14]. The largest cluster size detected in this study is 10-plet, and was found not to grow with increasing load (monitored to within 0.1% of final failure). Therefore, the definition of critical cluster size or more generally the critical nature of damage needed to trigger final failure does not appear to be a useful concept in our case although it maybe that critical clusters occur even closer to final fracture than could be captured here. In fact, the current generation of synchrotron radiation CT instruments do not allow observations with even higher temporal resolution (>20 Hz) and relatively large fields of view such as the one considered here. In addition, the concept of 'cluster' does not have a consistent definition in literature so that the comparison of results from different studies needs to be conducted carefully. Previous work has used the minimum axial distance measured between multiple breaks along the same fibre, *i.e.* the estimated ineffective length, to define the radius of the cluster region [7,15]. Based on this definition, all the breaks within a distance of less than the estimated ineffective length are considered to belong to the cluster regardless of whether they are co-planar, dispersed or adjacent to each other. The biggest cluster size detected by Scott *et al.* [15] was of a 14-plet and it occurred at 94% UTS. However, due to the fact that this was the last load level applied before failure, there is no evidence as to its growth. Thionnet *et al.* [11] developed a model to investigate a variety of loading conditions ranging from high speed monotonic load to sustained load, which highlighted differences in the accumulation of fibre fractures and cluster formation. In particular, they found that the effect of time is fundamental to the failure mode predicted by the model, showing random fibre failure and coalescence of clusters for high speed monotonic loading, while sustained loading exhibited early cluster formation [11]. Therefore, the 14-plet observed in previous study at 94% UTS [15] might be affected by the hold-at-load used to allow time for the CT scan, which might have not negligible influence at high loads. Previous models were unsuccessful in the prediction of

larger clusters at high loads [7,12]; however, this study has indicated that very high loads do not necessarily result in large cluster formation (*i.e.* coupon B).

Results found in this study have demonstrated a different behaviour between the two coupons considered, particularly in terms of clusters formation. Whatever the mechanism, these observations confirm the need to examine many specimens to assess stochastic behaviours where failure may be determined by extreme value statistics. While this study has involved just two specimens, it represents ~14,000 fibres under load, with a visualised gauge length of ~2 mm each, nevertheless events that appear to be potentially relevant to failure are distinctly sparse. For example, one individual 2 mm fibre length fractured 8 times and the neighbouring fibre 6 times, whilst none of the remaining 14,000 fibres failed more than 4 times.

5. Conclusions

The current work represents the first use of fast computed tomography to monitor the accumulation of fibre breaks in notched coupons immediately prior to fracture (up to 99.9% of the ultimate tensile stress). 4D (time lapse) observations have shown that new breaks are overwhelmingly associated with new locations rather than occurring preferentially adjacent to existing failed fibres. Their accumulation was demonstrated to follow a power law curve, with a substantial number of breaks (up to 35% of the total number detected) occurring in a limited load range immediately before failure, 98-99.9% UTS. The coupon that exhibited the higher number of breaks was also characterised by early cluster formation and multiple axial fragmentation, whilst failing at higher load. The different behaviour detected for the two coupons considered, particularly in terms of clusters formation, raises important observations on the need to consider potential microstructural and material variations at large length scales. The work presented in this paper should be of significance to the modelling community and lead to further improvement in the ability to predict the tensile strength and related performance of continuous carbon-fibre composite materials.

Acknowledgements

The authors acknowledge the Engineering and Physical Science Research Council (EPSRC) for funding the Henry Moseley X-ray Imaging Facility (grants EP/F007906/1, EP/F001452/1 and EP/I02249X/1). The authors are grateful to the Swiss Light Source for access to the TOMCAT-X02DA beamline and for the assistance of Dr. Rajmund Mokso. Many thanks are due to colleagues at INSA-Lyon MATEIS for providing the loading rig used in these experiments, particularly to Dr. Eric Maire for his support during the beamtime. Thanks to µ-VIS at the University of Southampton. Materials were supplied by Airbus SAS.

References

[1] M.J. Hinton and P.D. Soden, 'Predicting failure in composite laminates: the background to the exercise', Compos. Sci. Technol. 58, 1001-1010, 1998.
[2] J.M. Hedgepeth, 'Stress concentrations in filamentary structures', NASA TND882, Langley Research Center, 1961.
[3] J.M. Hedgepeth, P. Van Dyke, 'Local stress concentrations in imperfect filamentary composite materials', J. Compos. Mater. 1, 294-309, 1967.
[4] S.B. Batford, 'Tensile strength of unidirectionally reinforced composites I.', J. Reinf. Plast. Compos. 1, 153-163, 1982.
[5] S. Ochiai, K. Schulte, P.W.M. Peters, 'Strain concentration for fibers and matrix in unidirectional composite', Compos. Sci. Technol. 41, 237-256, 1991.
[6] I.J. Beyerlein, S.L. Phoenix, 'Stress concentrations around multiple fiber breaks in an elastic matrix with local yielding or debonding using quadratic influence superposition', J. Mech. Phys. Solids 44, 1997-2039, 1996.
[7] Y. Swolfs, H. Morton, A.E. Scott, L. Gorbatikh, P.A.S. Reed, I. Sinclair, S.M. Spearing, I. Verpoest, 'Synchrotron radiation computed tomography for experimental validation of a tensile strength model for unidirectional fibre-reinforced composites', Composite: Part A, Vol. 77, 106-113, 2015.
[8] B. Rosen, 'Tensile failure of fibrous composites', AIAA J, Vol. 2, pp.1985-91, 1964.
[9] C. Zweben, 'Tensile failure of fibers composites', AIAA J 6, 2325-31, 1968.
[10] C. Zweben, B.W. Rosen, 'A statistical theory of material strength with application to composite materials', J. Mech. Phys. Solids, Vol. 18, 189-206, 1970.
[11] A. Thionnet, H.Y. Chou and A. Bunsell 'Fibre break processes in unidirectional composites'. Composite: Part A, Vol. 65, 148-160, 2014.
[12] A.E. Scott, I. Sinclair, S.M. Spearing, A. Thionnet, A.R. Bunsell, 'Damage accumulation in a carbon/epoxy composite: comparison between a multiscale model and computed tomography experimental results', Composites: Part A, Vol. 43, 1514-1522, 2012.
[13] L. Mishnaevsky, P. Brondsted, 'Micromechanims of damage in unidirectional fibre reinforced composites: 3D computational analysis', Compos. Sci. Technol. 69, 1036-1044, 2009.
[14] R.L. Smith, S.L. Phoenix, M.R. Greenfield, R. B. Henstenburg, R.E. Pitt, 'Lower-Tail approximations for the probability of failure of three-dimensional fibrous composites with hexagonal geometry', Proceedings of the Royal Society of London. Series A, Mathematical and Physical Sciences, Vol. 388, 353-391, 1983.
[15] A.E. Scott, M. Mavrogordato, P. Wright, I. Sinclair and S.M. Spearing, 'In situ fibre fracture measurement in carbon-epoxy laminates using high resolution tomography', Compos. Sci. Technol. 71, 1471-1477, 2011.
[16] E. Maire and P.J. Withers, 'Quantitative X-ray tomography', Int. Mater. Rev. 59, 1-43, 2014.
[17] P. Wright, A. Moffat, I. Sinclair, S.M. Spearing, 'High resolution tomographic imaging and modelling of notch tip damage in a laminated composite', Compos. Sci. Technol. 70, 1444-1452, 2010.

[18]R. Mokso, F. Marone, S. Irvine, M. Nyvlt, D. Schwyn, K. Mader, G.K. Taylor, H.G. Krapp, M. Skeren and M. Stampanoni, 'Advantages in phase retrieval for fast x-ray tomographic microscopy', J. Phys. D: Appl. Phys 46, 1-12, 2013.
[19] R. Mokso, D.A. Schwyn, S.M. Walker, M. Doube, M. Wicklein, T. Muller, M. Stampanoni, G.K. Taylor, H.G. Krapp, 'Four-dimensional in vivo X-ray microscopy with projection-guided gating', Sci. Rep. 5, 8727, 2015.
[20]E. Maire, C. Le Bourlot, J. Adrien, A. Mortensen, R. Mokso, '20 Hz X-ray tomography during an in situ tensile test', Int. J. Frac., 3-12, 2015.
[21]Hexcel HexPly M21. http://www.hexcel.com/Resources/DataSheets/Prepreg-Data-Sheets/M21_global.pdf
[22]S.C. Garcea, M.N. Mavrogordato, A.E. Scott, I. Sinclair, S.M. Spearing, 'Fatigue micromechanism characterisation in carbon fibre reinforced polymers using synchrotron radiation computed tomography', Compos. Sci. Technol. 99, 23-30, 2014.
[23]P.M. Wright, 'Investigation of damage in laminated carbon fibre composites using high resolution computed tomography', PhD Thesis, University of Southampton; 2011.
[24]B. Yu, R.S. Bradley, C. Soutis and P.J. Withers, 'A comparison of different approaches for imaging cracks in composites by X-ray microtomography', Phil. Trans. R. Soc. A 374, 2016.
[25]S.C. Garcea, I. Sinclair, S.M. Spearing, 'Fibre failure assessment in carbon fibre reinforced polymers under fatigue loading by synchrotron X-ray computed tomography', Compos. Sci. Technol. 133, 157-164, 2016.
[26]D. Paganin, S.C. Mayo, T.E. Gureyev, P.R. Miller, S.W. Wilkins, 'Simultaneous phase and amplitude extraction from a single defocused image of a homogeneous object', Journal of Microscopy 206, 33-40, 2002.
[27]B.A. Dowd, G.H. Campbell, R.B. Marr, V. Nagarkar, S. Tipnis, L. Axe and D.P. Siddons 'Developments in synchrotron x-ray computed tomography at the National Synchrotron Light Source'. Proc. SPIE 3372, 224-236, 1999.
[28]K.M. Jespersen, J. Zangenberg, T. Lowe, P.J. Withers, L. P. Mikkelsen, 'Fatigue damage assessment of uni-directional non-crimp fabric reinforced polyester composite using X-ray computed tomography', Compos. Sci. Technol. 136, 94-104, 2016.
[29] J. Zangenberg, P. Brøndsted, J. W. Gillespie, 'Fatigue damage propagation in unidirectional glass fibre reinforced composites made of a non-crimp fabric', Journal of Composite Materials 48, 2711-2727, 2014.
[30]S. Deng, L. Ye, Y-W Mai and H-Y Liu, 'Evaluation of fibre tensile strength and fibre/matrix adhesion using single fibre fragmentation tests', Composite: Part A 29, 423-434, 1998.
[31]C. Marston, B. Gabbitas, J. Adams and S. Nutt, 'Failure characteristics in carbon/epoxy composite tows', Composite: Part A 27, 1183-1194, 1996.
[32]X. Ji, X-R. Liu and T-W Chou, 'Dynamic stress concentration factors in unidirectional composites', J. Compos. Mater. 19, 269-275, 1985.
[33]M.L. Accorsi, A. Pegoretti, A.T. Dibenedetto, 'Dynamic analysis of fibre breakage in single and multiple-fibre composites', J. Mater. Sci 31, 4181-4187, 1996.
[34]G. Bullegas, S.T. Pinho and S. Pimenta 'Engineering the translaminar fracture behaviour of thin-ply composites'. Compos. Sci. Technol. 131, 110-122, 2016.
[35]M. Mirkhalaf, A. Khayer Dastjerdi and F. Barthelat, 'Overcoming the brittleness of glass through bio-inspired and micro-architecture'. Nat. Commun. 5, 2014.

Table Caption

Table 1 Summary of fibre breaks observed as a function of the percentage of UTS and load for coupons A and B.

Figure Captions

Fig. 1 3D rendering of the notch region 1s prior to final failure (99.9% UTS) segmented to show the various damage modes (rendered with different colours).
Fig. 2 Cross-section of a slice parallel to the loading direction reconstructed under (a) absorption mode, (b) Paganin mode and (c) median filtering of the absorption mode image.

Fig. 3 Cross-section of a slice parallel to the loading direction for the same position in the coupon: at (a) 55% UTS, (b) 85% UTS, and (c) 99.9% UTS.

Fig. 4 Projection of failed fibre in the 0˚ plies into a plane parallel to the loading direction and through the laminate thickness for the load of 99.9% UTS: (a) coupon A and (b) coupon B.
Fig. 5 Total number of fibre breaks detected as a function of the nominal stress in the load-bearing reduced cross section for the two coupons considered. The dashed lines represent the power law best fits to the experimental results.
Fig. 6 Percentage of fibre breaks occurring as clusters for different levels of the UTS for: (a) coupon A, and (b) coupon B, divided as singlets and multiple breaks (c-d).
Fig. 7 Cross-section parallel to the loading direction for the same position in the coupon at: (a) 9 s, (b) 8 s, and (c) 1 s before final failure.
Fig. 8 Images of a 2D slice parallel to the loading direction at incremental UTS showing the development of multiple fractures along a single fibre.
Fig. 9 2D slice parallel to the loading direction at incremental UTS showing the fragmentation sequence along a single fibre as splitting of the initial fragment.
Fig. 10 Cumulative distribution of the fragment lengths formed by multiple fibre breaks along individual fibres, obtained considering all of the fibres exhibiting multiple breaks in the two coupons.
Fig. 11 Cross-sections along the loading direction for a fibre that exhibited 8 breaks.

Figure 1

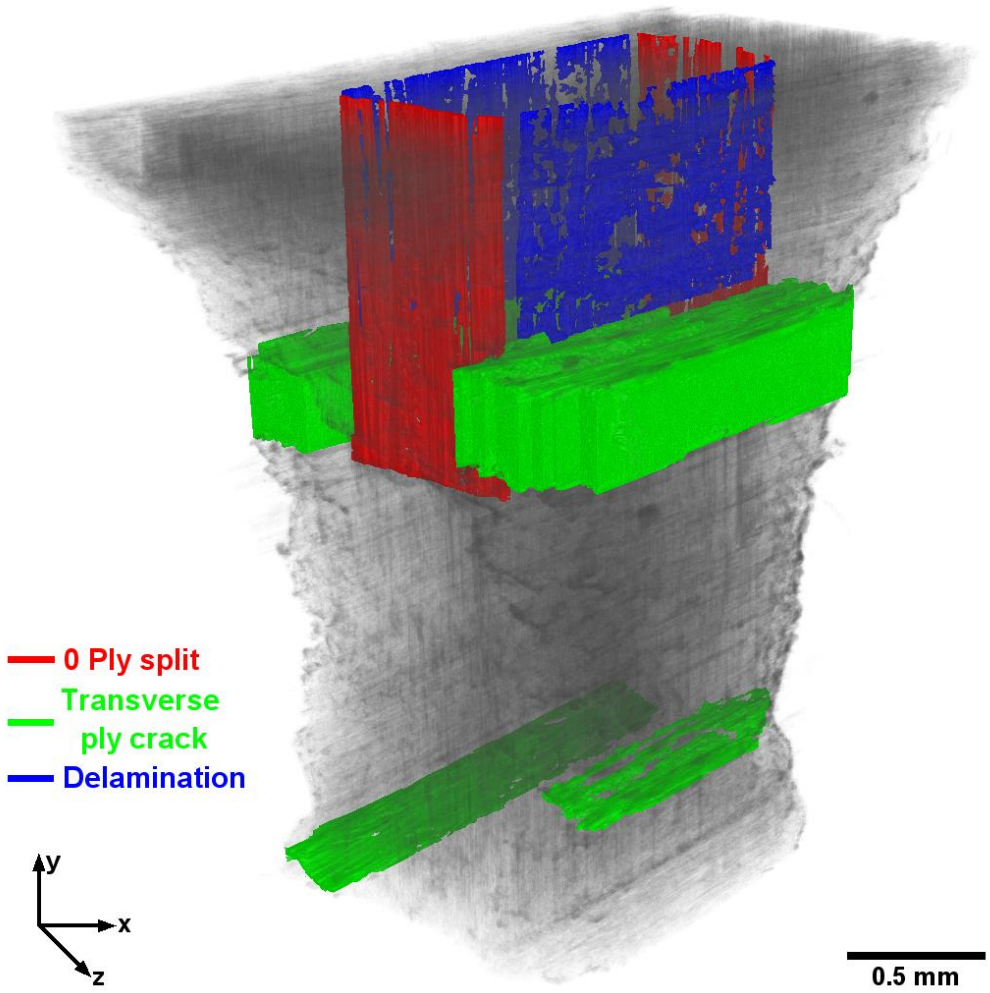

Figure 2

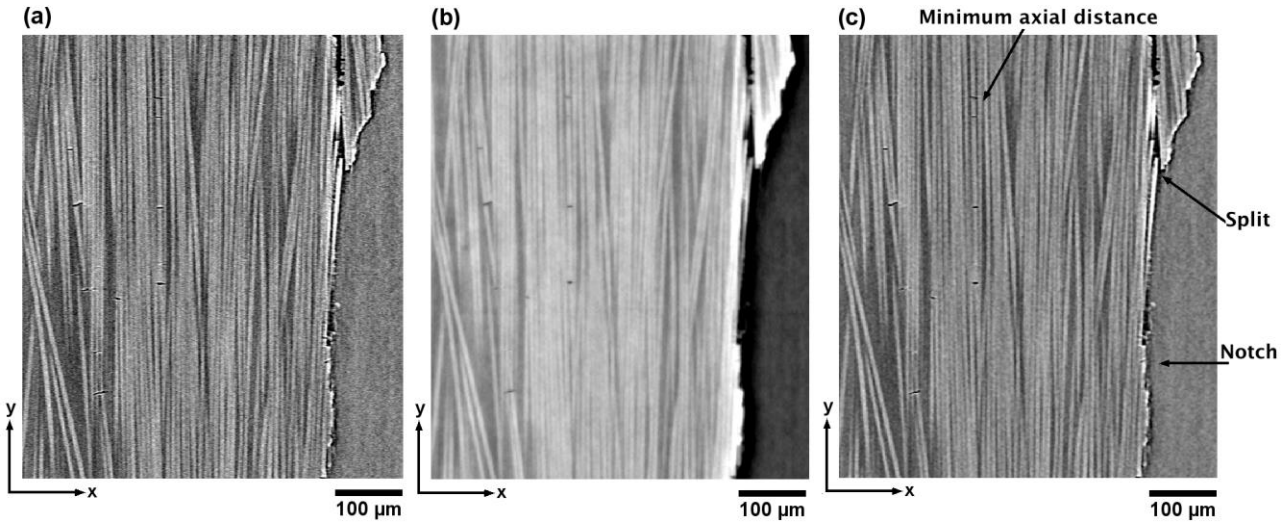

Figure 3

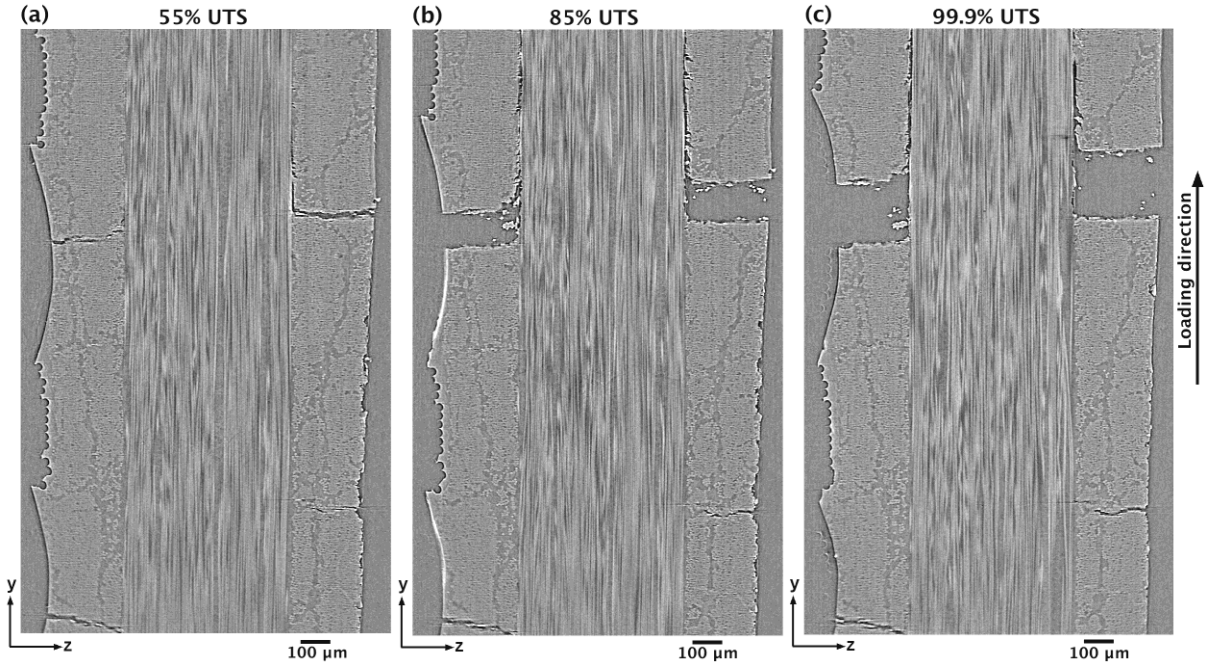

Figure 4

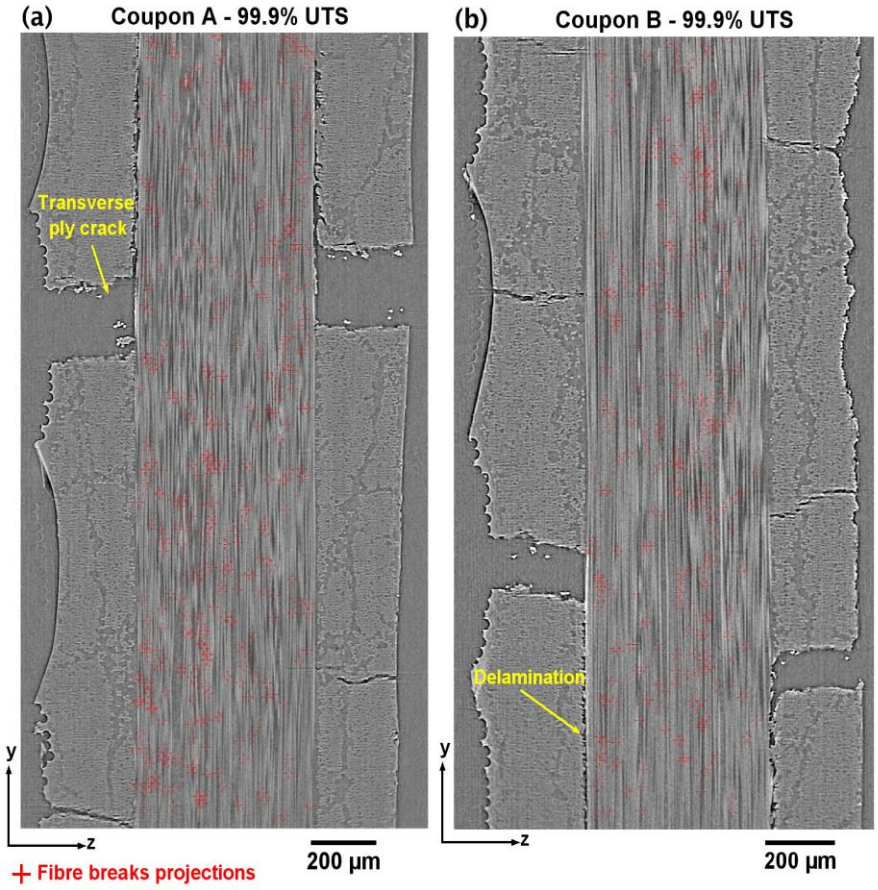

Figure 5

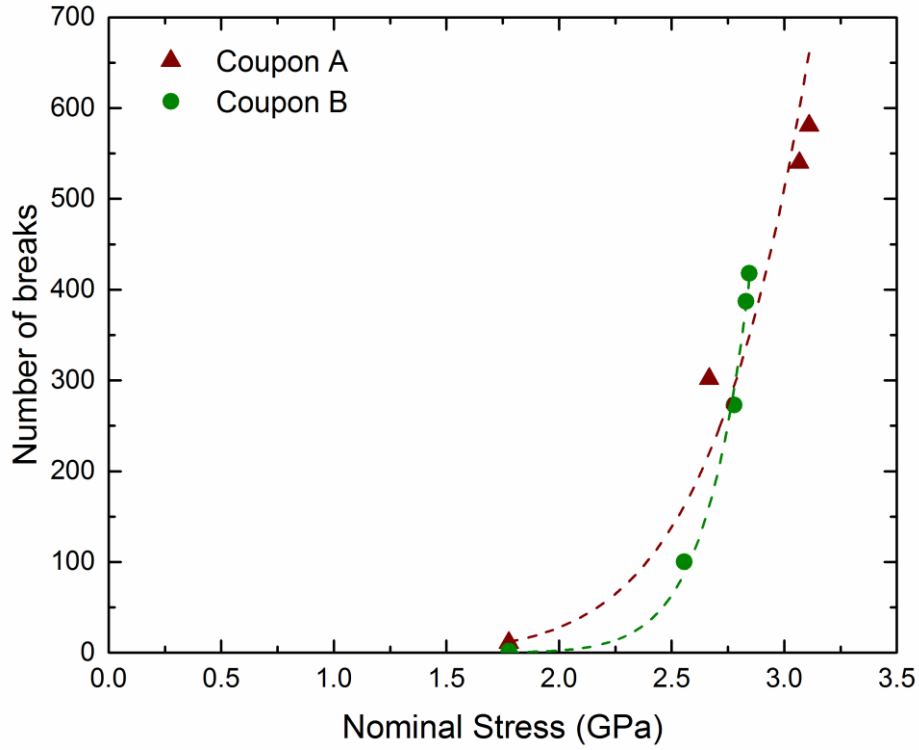

Figure 6

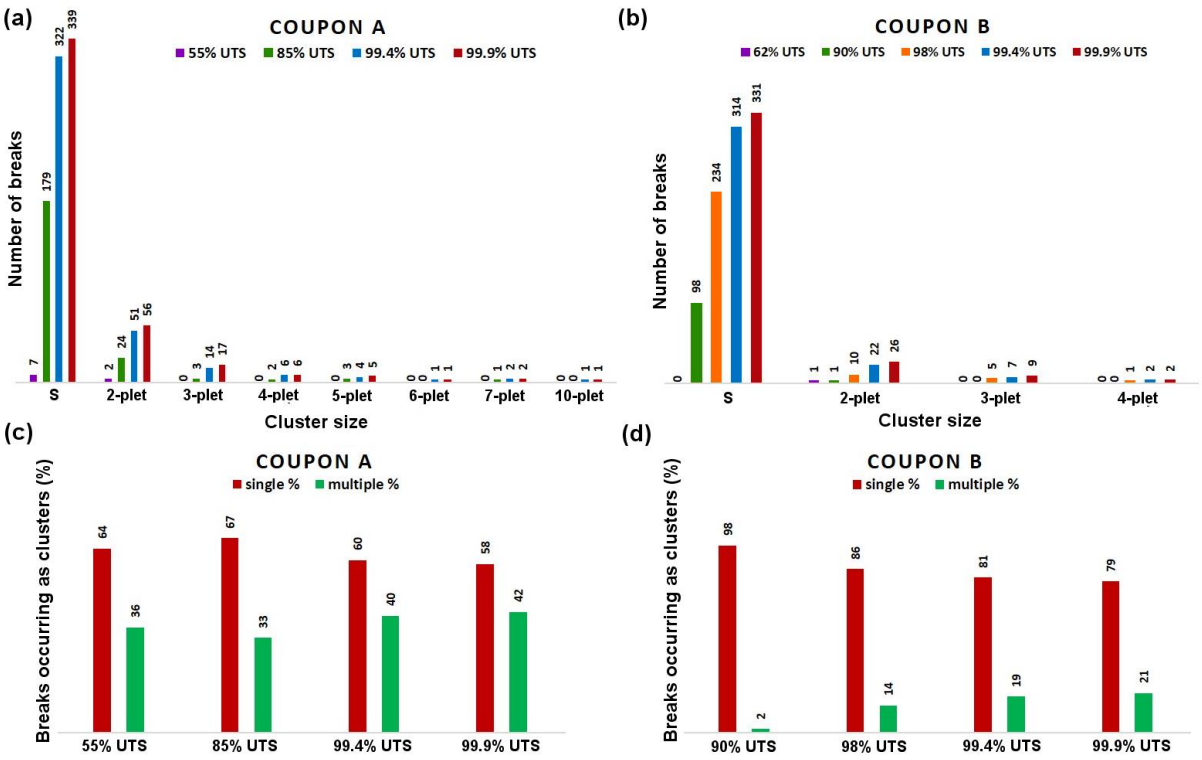

Figure 7

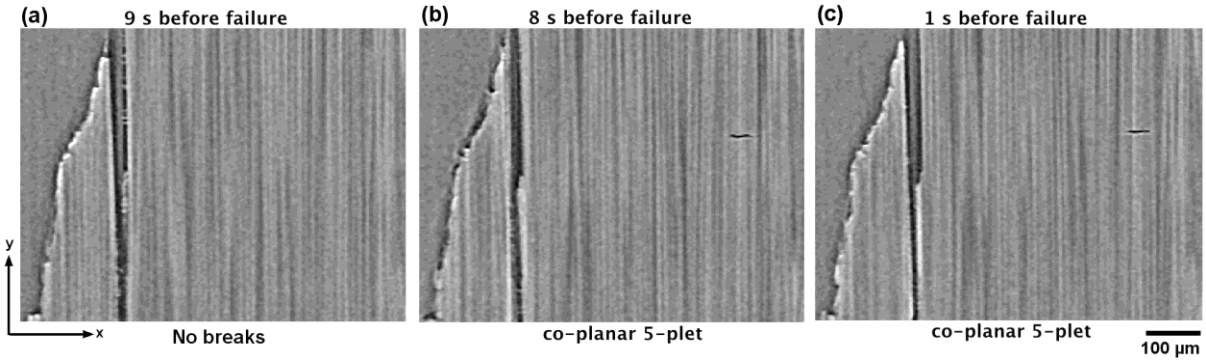

Figure 8

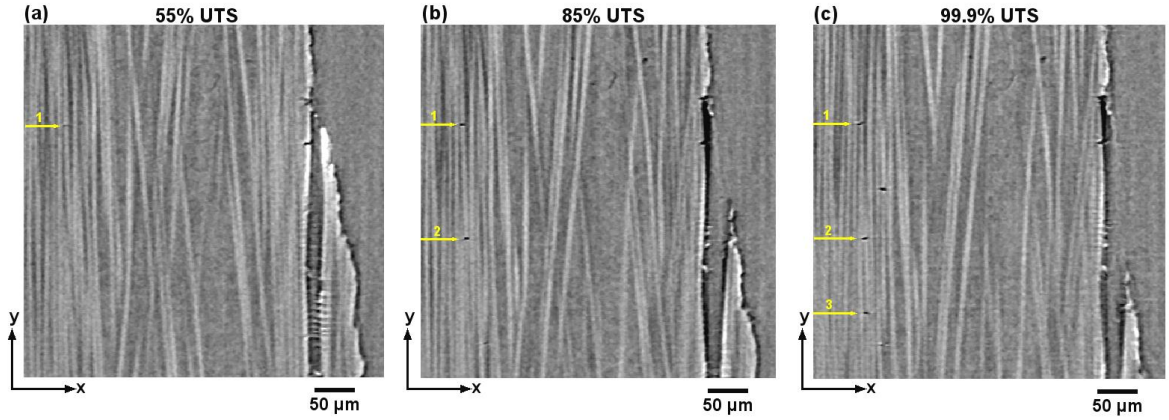

Figure 9

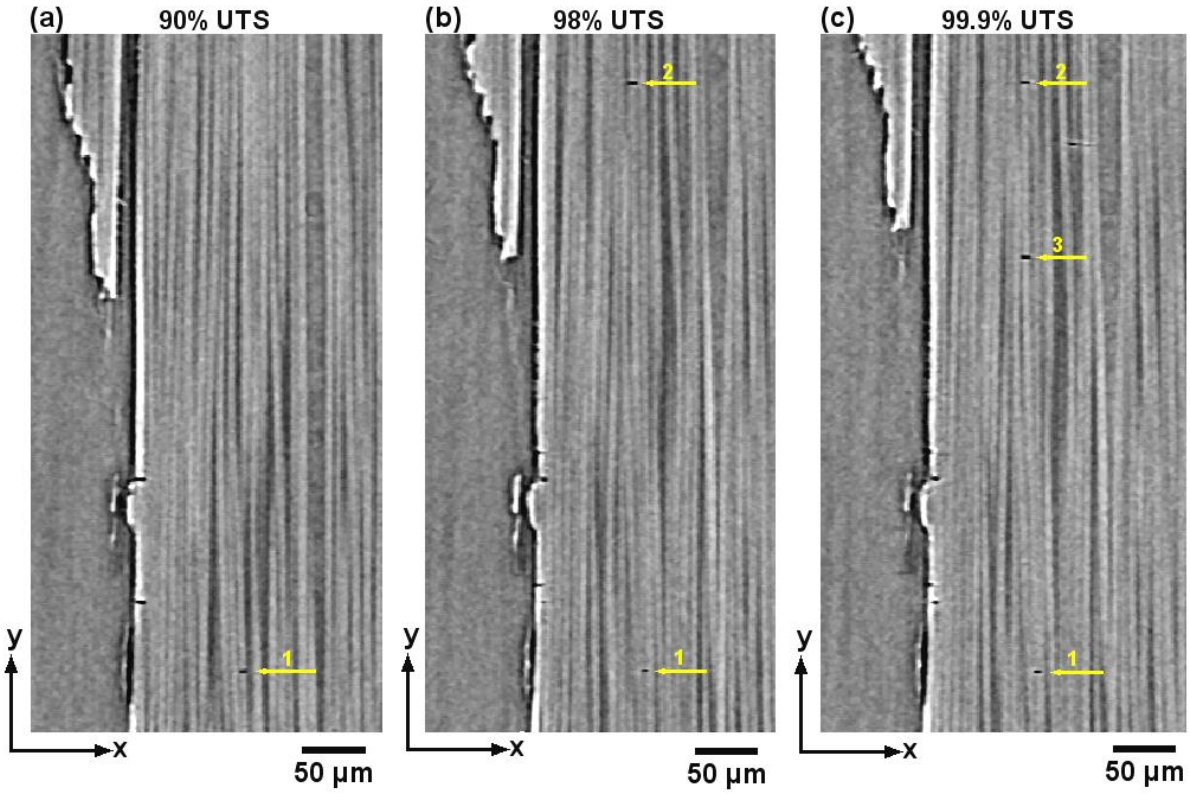

Figure 10

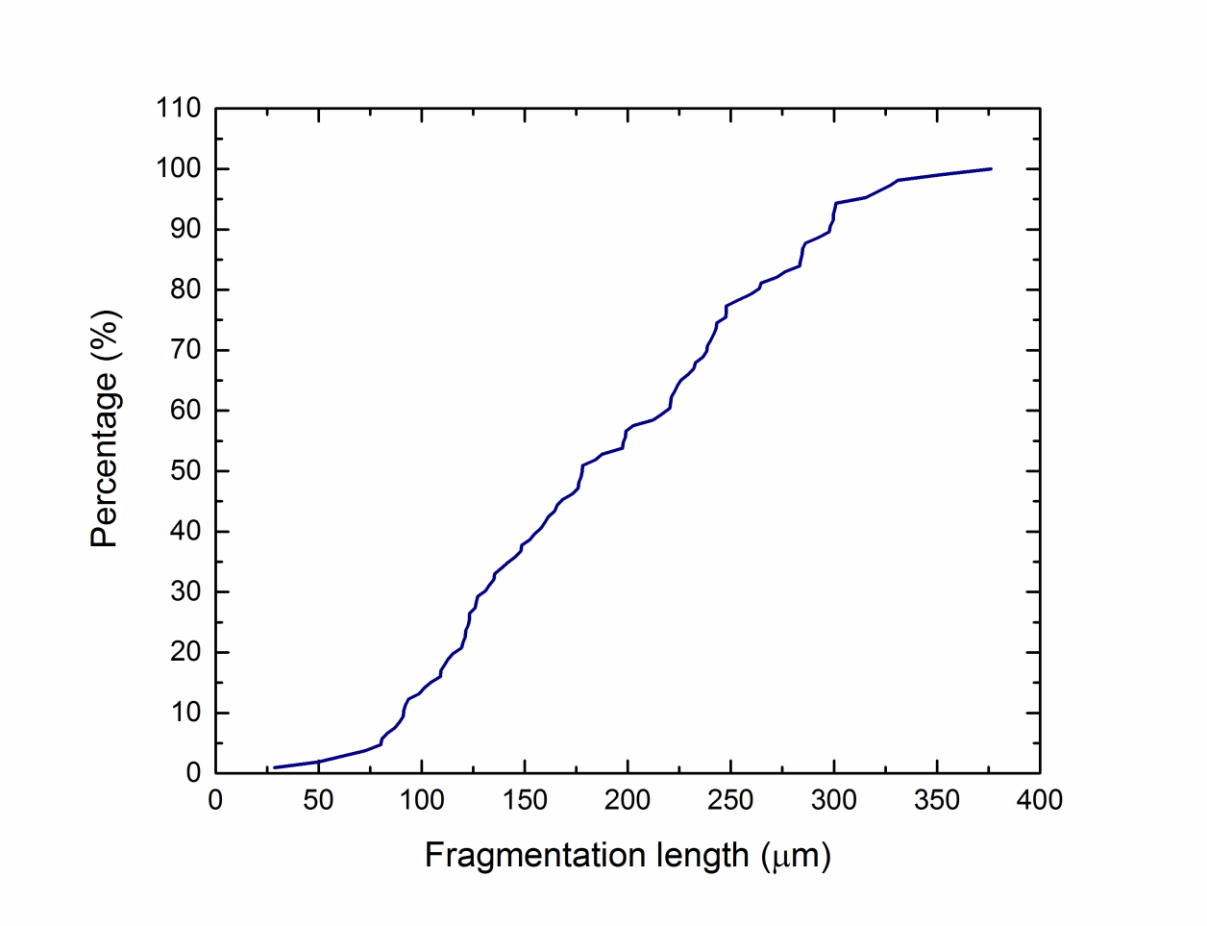

Figure 11